Supporting Information

Anti-Kasha's rule in phenothiazine derivatives and metal-organic frameworks: mechanism investigation and application in hypochlorite detection

Tingting Wu,[a] Mingyuan Lei,[a,b] Fayuan Ge,[a] Yang Liu,[a] Minqi Xia,[c] Lijun Yang[c] and Hegen Zheng[*a]

[a]State Key Laboratory of Coordination Chemistry, School of Chemistry and Chemical Engineering, Collaborative Innovation Center of Advanced Microstructures, Nanjing University, Nanjing 210023, Jiangsu, P. R. China. E-mail: zhenghg@nju.edu.cn
[b]Key Laboratory of Evidence Identification in Universities of Shandong Province, Shandong University of Political Science and Law, Jinan, Shandong 250014, P R China.
[c]Key Laboratory of Mesoscopic Chemistry of MOE and Jiangsu Provincial Laboratory for Nanotechnology, School of Chemistry and Chemical Engineering, Nanjing University, Nanjing 210023, Jiangsu, P R China.

General Information

NMR spectra were measured on a Bruker Avance 500 MHz NMR spectrometer (^{1}H: 500 MHz) and Bruker Avance 400 MHz NMR spectrometer (^{1}H: 400 MHz). Powder X-ray diffraction (PXRD) data were recorded on a Bruker D8 ADVANCE X-ray powder diffractometer (Cu Kα, λ = 1.54056 Å). Thermogravimetric analyses (TGA) were performed with a Netzche STA449F3 thermogravimetric analyzer with a heating rate of 10 °C min^{-1} under a N_2 atmosphere upon heating from room temperature to 600 °C. The photoluminescence spectra were obtained by Horiba Jobin Yvon Fluorolog-3 spectrofluorometer and Edinburgh FLS920. The UV-vis absorption spectra were analyzed by SHIMADZU UV3600. For femtosecond-resolved TA measurement, a Ti:sapphire regenerative amplifier (90 fs, 1 kHz, Libra, Coherent Inc.) was used for TA spectroscopy. An optical parametric amplifier (OperA Solo, Coherent Inc.) pumped by the regenerative amplifier was used to generate the pump beam at the wavelengths of 355 nm and 700 nm. And the probe beam is a broadband supercontinuum light source generated by focusing a small portion of the femtosecond laser beam onto either a 3 mm-thick sapphire plate for visible range. The TA signal was then analyzed by a silicon CCD (S11071, Hamamatsu) mounted on a monochromator (Acton 2358, Princeton Instrument) at 1 kHz enabled by a custom-built control board from Entwicklungsbuero Stresing. The Fourier transform infrared (FT-IR) spectra were recorded with a VERTEX70 spectrometer in the range 4000-400 cm^{-1}. The HRMS spectrum was measured on Agilent 6540 accurate-mass quadrupole time-of-flight (Q-TOF) mass spectrometer equipped with an electrospray ionization (ESI) source in positive ionization mode. X-ray photoelectron spectroscopy was analyzed by ULVAC-PHI PHI5000 VersaProbe. Cyclic voltammetry (CV) was carried out on a CHI voltammetric analyzer in a threeelectrode cell with a Pt counter electrode, a Ag/AgCl reference electrode, and a glassy carbon working electrode at a scan rate of 100 mVs^{-1} with 0.1 M tetrabutylammonium hexafluorophosphate, in anhydrous dichloromethane solution purged with nitrogen. The morphology of the samples was analyzed by Shimadzu SSX-550 scanning electron microscope (SEM).

All chemicals and solvents were used without further purification.

Syntheses of H$_2$PTZ-dba

3,7-dibromo-10*H*-phenothiazine was synthesized as described by Xiao-Qing Zhu, *et al*.[S1] 10*H*-Phenothiazine (1.99 g ,10 mmol) was suspended in glacial acetic acid (120 mL) and a solution of bromine in glacial acetic acid (100mL, 10% v/v, 40 mmol) was added dropwise with continuous stirring to yield 3,7-dibromo-10*H*-phenothiazine as green crystals (2.92 g, yield 82%). The mixture of 3,7-dibromo-10*H*-phenothiazine (1.77 g, 5 mmol), (4-(ethoxycarbonyl)phenyl)boronic acid (2.91 g, 15 mmol), tetratriphenylphosphine palladium (0.135 mmol, 156 mg) and anhydrous potassium carbonate (15 mmol, 2.07 g) in toluene (60 mL), 1,4-dioxane (60 mL) and water (60 mL) were stirred under a N_2 atmosphere at 120 °C for 8 h. When the reaction was cooled down, removing the solvent and extracting it with ethyl acetate and water, the organic phase was dried and then evaporated to gain brown solid. By the recrystallization of toluene and ethanol, 2.3 g of PTZ-dbOEt (yellow solid, yield 93%) was obtained. PTZ-dbOEt (5 g, 1.01 mmol) in THF (60 mL) and ethanol was added in 2 M NaOH aqueous solution (60 mL, 120 mmol) and the system was reflexed for 16 h. After the reaction was finished, the mixture was acidified with concentrated HCl. The precipitate was collected by filtration, washed with water and then dried to give H$_2$PTZ-dba (4.268 g, yield = 97%) as a

yellow solid.^{1}H NMR (500 MHz, DMSO-d_6): δ = 12.91 (s, 2H), 9.01 (s, 1H), 7.96 (d, J= 2.5 Hz, 4H), 7.73 (d, J= 2.5 Hz, 4H), 7.42 (d, J= 5 Hz, 2H), 7.36 (s, 2H), 6.78 (d, J= 5 Hz, 2H).
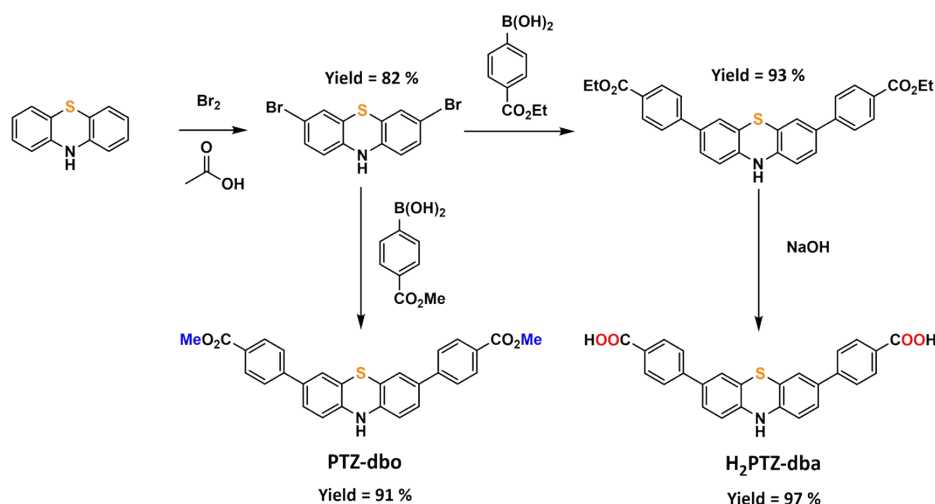
Syntheses of PTZ-dbo

The mixture of 3,7-dibromo-10H-phenothiazine (1.77 g, 5 mmol), (4-(methoxycarbonyl)phenyl)boronic acid (2.70 g, 15 mmol), tetratriphenylphosphine palladium (0.135 mmol, 156 mg) and anhydrous potassium carbonate (15 mmol, 2.07 g) in toluene (60 mL), 1,4-dioxane (60 mL) and water (60 mL) were stirred under a N_2 atmosphere at 120 °C for 8 h. When the reaction was cooled down, removing the solvent and extracting it with ethyl acetate and water, the organic phase was dried and then evaporated to gain brown solid. By the recrystallization of toluene and ethanol, 2.12 g of **PTZ-dbo** (yellow solid, yield 91%) was obtained. ^{1}H NMR (400 MHz, DMSO-d_6): δ = 9.02 (s, 1H), 7.95 (d, J= 2.5 Hz, 4H), 7.76 (d, J= 2.5 Hz, 4H), 7.42 (d, J= 5 Hz, 2H), 7.36 (d, J= 5 Hz, 2H), 6.77 (s, 2H), 3.86 (s, 6H).

The crystals analyzed by SCXRD were gained by following steps: Dissolve **PTZ-dbo** (8 mg, 0.017 mmol) and Pb(NO$_3$)$_2$ (20mg, 0.06 mmol) in the mixture of 4 mL of DMA and 300μL HCl (1M) by ultrasound. The suspension was sealed and heated at 100 °C for 72 h and then cooled to room temperature. The yellow crystal was collected (yield of 95% based on **PTZ-dbo**). Elemental analysis for evacuated samples of **PTZ-dbo** (C$_{28}$H$_{21}$NO$_4$S): C, 71.94; H, 4.49; N, 2.99; %. Found: C, 70.86; H, 4.51; N, 2.95 %.

Syntheses of Cd-PTZ-db

Dissolve H$_2$PTZ-dba (5 mg, 0.011 mmol) and Cd(NO$_3$)$_2$·4H$_2$O (10mg, 0.042 mmol) in the mixture of 3 mL of DMA and 1 mL of H$_2$O by ultrasound. The suspension was sealed and heated at 110 °C for 72 h and then cooled to room temperature. The yellow crystal was collected (yield of 90% based on H$_2$PTZ-dba). Elemental analysis for evacuated samples of **Cd-PTZ-db** (C$_{26}$H$_{19}$NCdO$_6$S): C, 53.25; H, 3.24; N, 2.38 %. Found: C, 52.78; H, 3.29; N, 2.37%.

Scheme S1 The synthesis strategy of **PTZ-dbo** and H$_2$PTZ-dba.

Single-crystal X-ray crystallography

The crystals of **PTZ-dbo** and **Cd-PTZ-db** were taken from the mother liquid without further treatment and mounted on MicroMesh (MiTeGen) with paratone oil at 193 K under a nitrogen cryostream. Single-crystal X-ray diffraction data of **PTZ-dbo** and **Cd-PTZ-db** were recorded on

a BRUKER D8 Venture diffractometer with graphite monochromated Ga Kα radiation (λ = 1.34138 Å). The SAINT program was used for the integration of the diffraction data and the intensity correction for the Lorentz and polarization effects.[S2] Semiempirical absorption correction was applied using the SADABS program.[S3] The structures were solved by direct method using SHELXS-2014,[S4] and the non-hydrogen atoms were refined on F^2 by full-matrix least-squares procedures with SHELXL-2018.[S5] All non-hydrogen atoms were refined anisotropically. The hydrogen atoms attached to carbons and nitrogen of ligand were generated geometrically with the riding model. The other hydrogen atoms of water molecules were located in difference Fourier maps and was also refined in the riding model approximation with O–H distance restraint (0.85(1) Å) and $U_{iso}(H) = 1.5U_{eq}(O)$. Crystallographic data in CIF format of **PTZ-dbo** and **Cd-PTZ-db** have been deposited in the Cambridge Crystallographic Data Centre (CCDC) under deposition CCDC numbers: 2303468 and 2303469. The details of crystal parameters, data collection, and refinements for **PTZ-dbo** and **Cd-PTZ-db** are summarized in Table S3. Selected bond lengths and angles are given in Table S4 and S5.

Theoretical calculations

Theoretical calculations were performed by Gaussian16[S6] to investigate the luminescent property of **PTZ-dbo**. Geometries of ground and excited states was optimized at LC-BLYP/def2-TZVP level. The solid-state environment was taking into account by tuning the range-separation parameter ω[S7]. For our system, ω and J^2 was optmized as 0.18433 Bohr^{-1} and 2.7934$\times$10^{-6}, respectively. The dielectric constant ε of solid **PTZ-dbo** was evaluated by molecular dynamics, which were performed by Gromacs 2019.6[S8]. A box containing 1000 **PTZ-dbo** molecules was relaxed and simulated using Gromos54A7 forcefield[S9] in NVT ensemble, where temperature and pressure were set as 298.15 K and 1 bar, respectively.
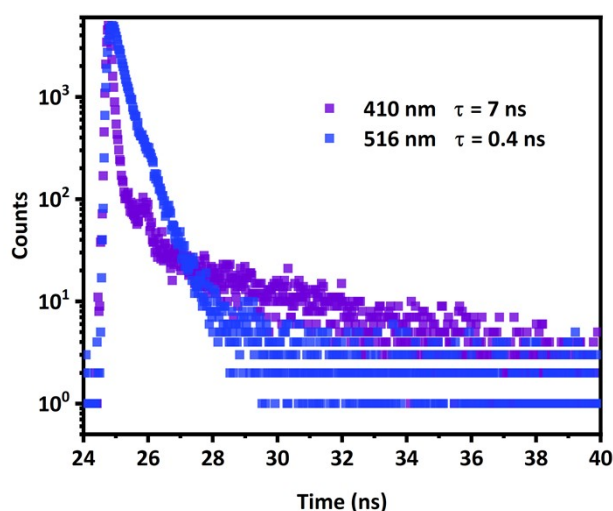
Results and discussion

Fig. S1 Time-resolved fluorescence decay curves of **PTZ-dbo** monitored at 410 nm and 516 nm at 298 K. λ_{ex} = 350 nm
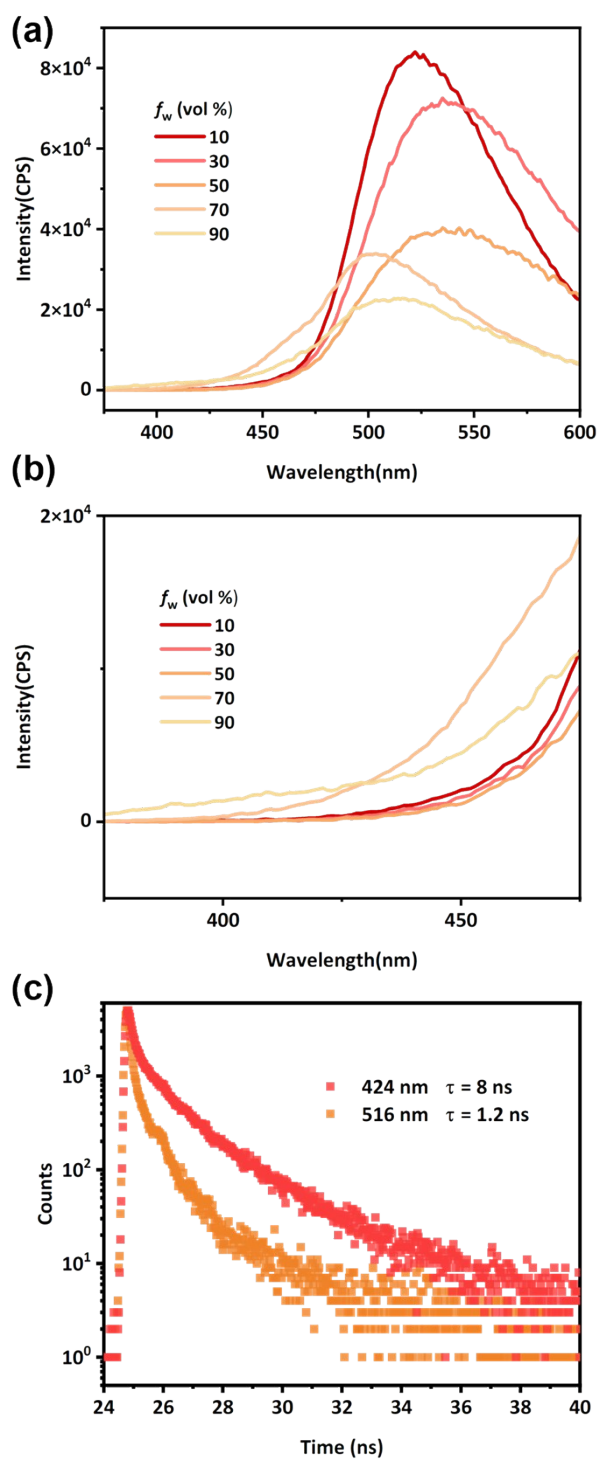

Fig. S2 (a) The PL spectra of H_2PTZ-dba in different solvents with 350 nm excitation; (b) selected part of (a). (c) Time-resolved fluorescence decay curves of H_2PTZ-dba monitored at 424 nm and 516 nm at 298 K. λ_{ex} = 350 nm
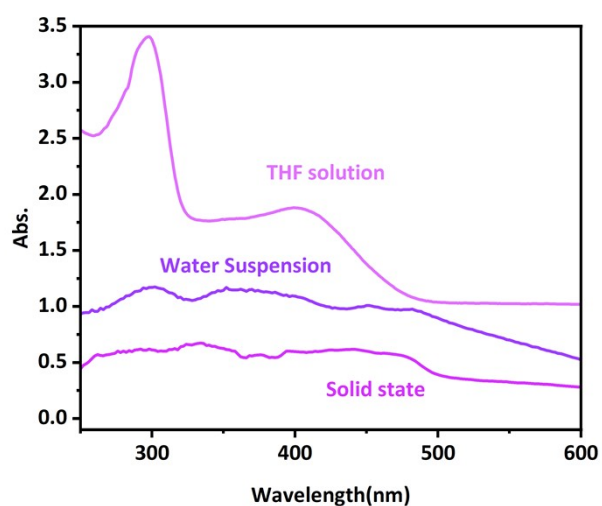
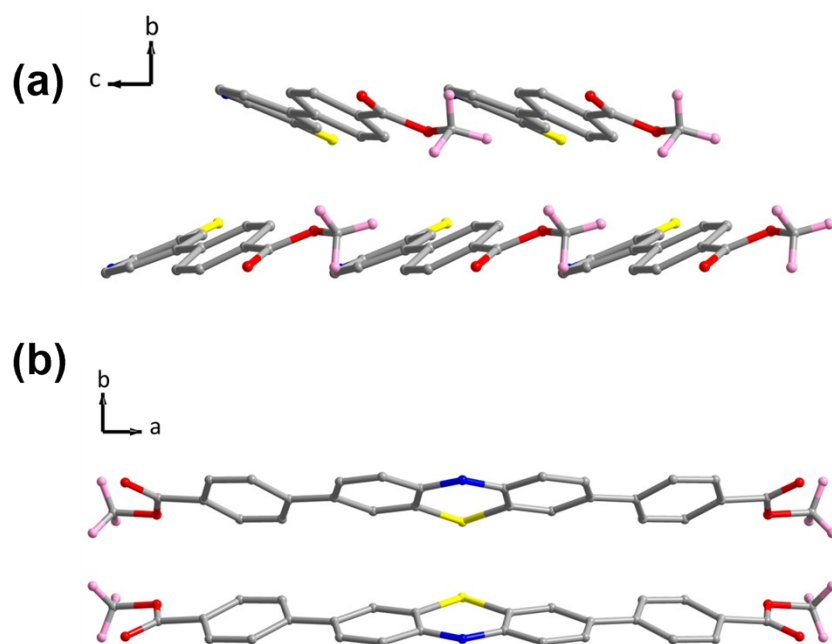**Fig. S3** The absorption spectra of **PTZ-dbo** in THF, water and solid state.

Fig. S4 The structure of **PTZ-dbo** seen form *a*-axis (a) and *c*-axis (b). (The hydrogen atoms connected to carbons and nitrogen atoms have been omitted for the sake of clarity. Color code: C, grey; O, red; N, blue; S, yellow; Cd, cyan)
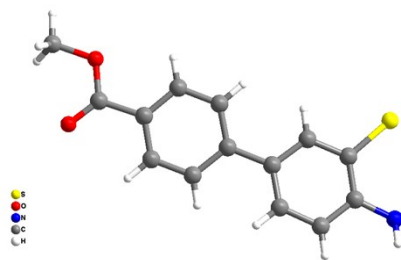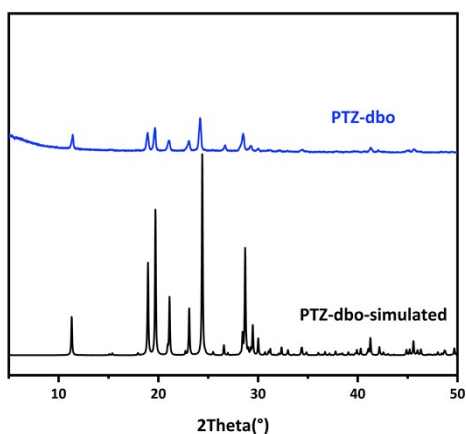
Fig. S5 The asymmetric unit of **PTZ-dbo**.

Fig. S6 PXRD patterns of **PTZ-dbo** powder.

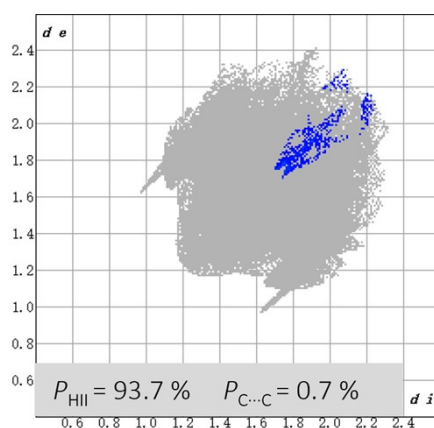$P_{HII} = 93.7\%$ $P_{C\cdots C} = 0.7\%$

Fig. S7 The decomposed fingerprint plots of Hirshfeld surfaces of intermolecular C···C interaction of **PTZ-dbo**. The full fingerprints appear as gray shadows underneath decomposed plots, and the intermolecular interaction is shown as a blue shadow. P_{HII} = proportion of hydrogen-involved intermolecular interaction to total intermolecular interaction; $P_{C\cdots C}$ = proportion of intermolecular C···C interaction to total intermolecular interaction.

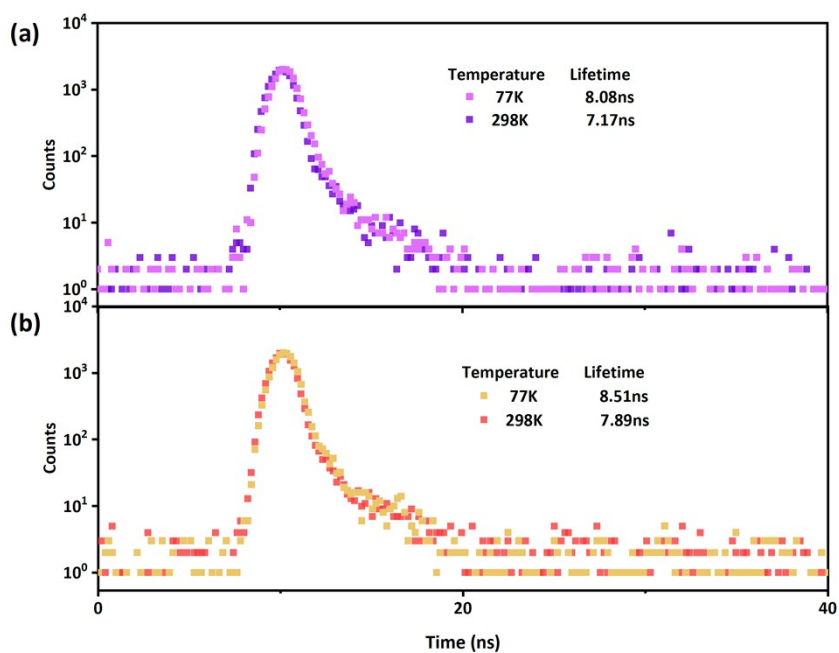**Fig. S8** Time-resolved fluorescence decay curves of (a) **PTZ-dbo** and (b) H_2PTZ-dba monitored at 400 nm at 298 K and 77 K. λ_{ex} = 350 nm
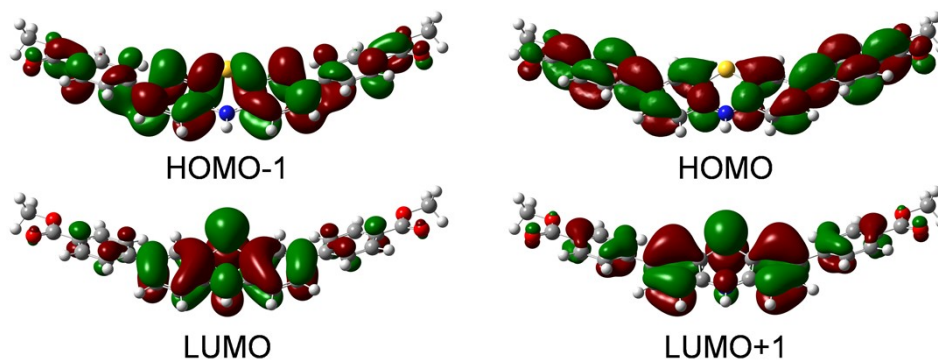

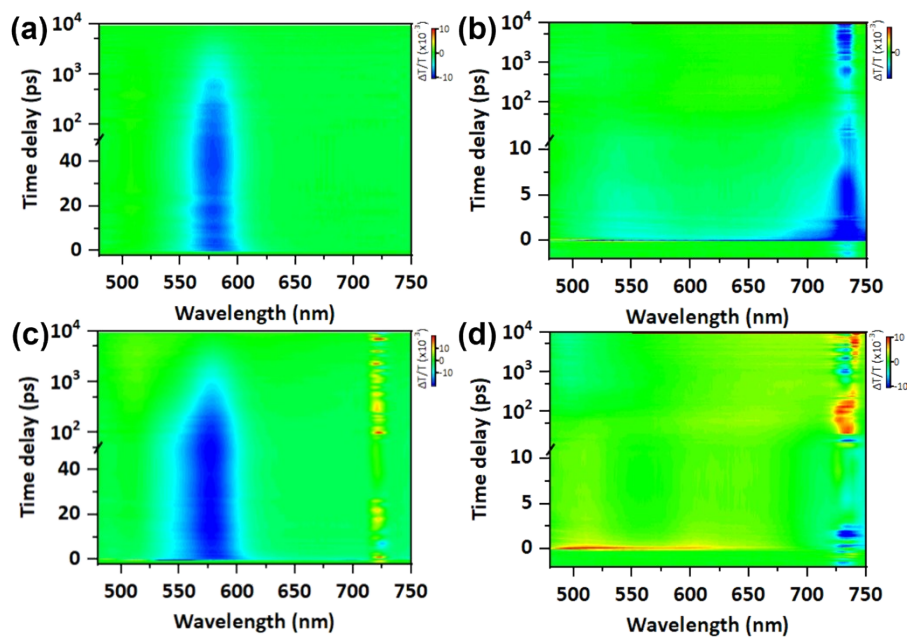**Fig. S9** The frontier orbitals of **PTZ-dbo**.

Fig. S10 The fs-TA profiles for H$_2$PTZ-dba in THF (a) and in the film state (b), **PTZ-dbo** in THF (c) and in the film state (d) with 355 nm excitation.
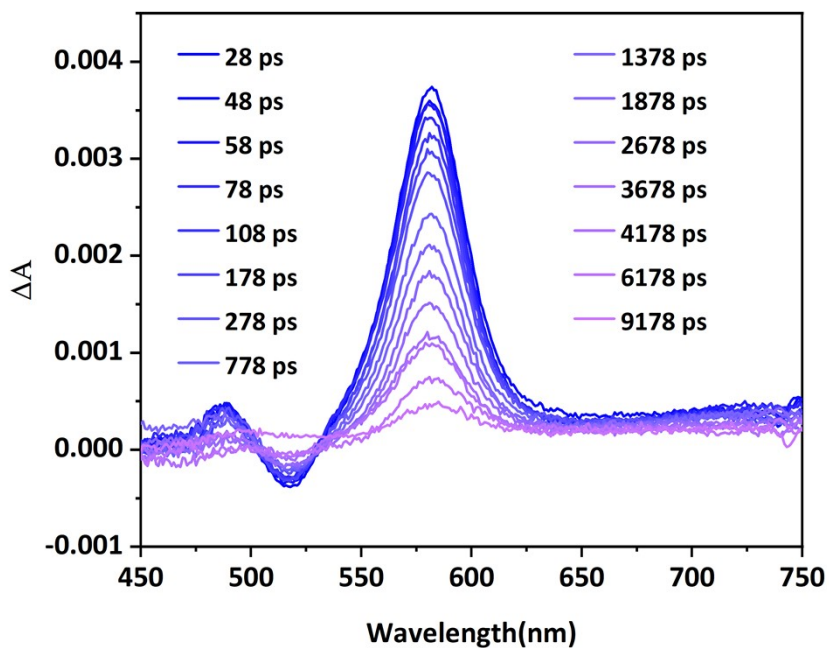

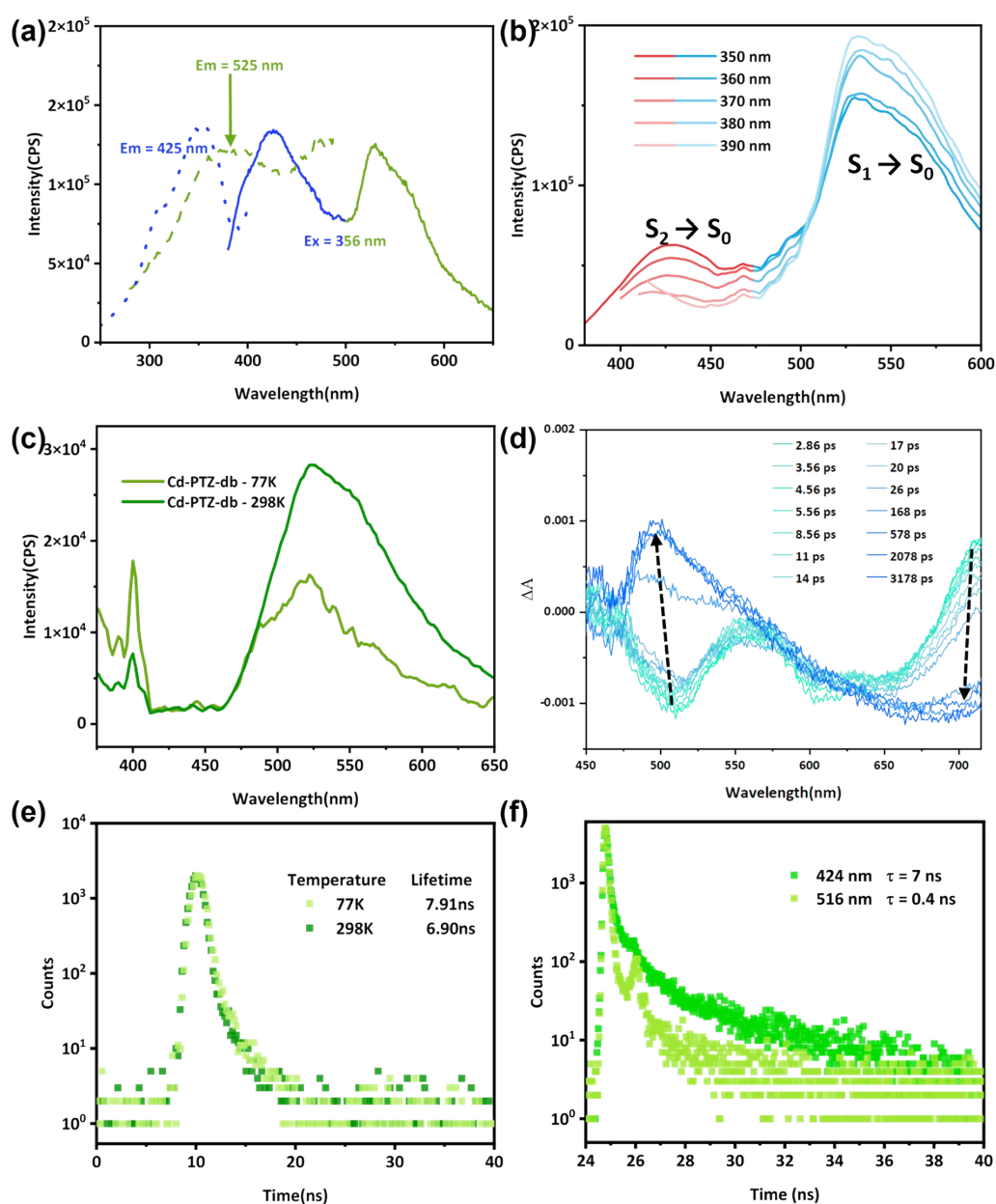**Fig. S11** The fs-TA spectra **PTZ-dbo** in THF with 355 nm excitation.

Fig. S12 (a) Excitation spectra of Cd-PTZ-db from emissions monitored at 425 nm (blue dashed line) and at 525 nm (green dashed lines); emission spectra (solid lines) in the water of **Cd-PTZ-db** (λ_{ex}=356 nm); (b) excitation-wavelength-dependent PL spectra of **Cd-PTZ-db** in water; (c) the solid PL spectra of Cd-PTZ-db at different temperature; (d) fs-TA spectra of Cd-PTZ-db in the film state with 355 nm excitation; (e) time-resolved fluorescence decay curves of **Cd-PTZ-db** solid monitored at 400 nm at 298 K and 77 K; (f) time-resolved fluorescence decay curves of **Cd-PTZ-db** in water monitored at 424 nm and 516 nm at 298 K. λ_{ex} = 350 nm
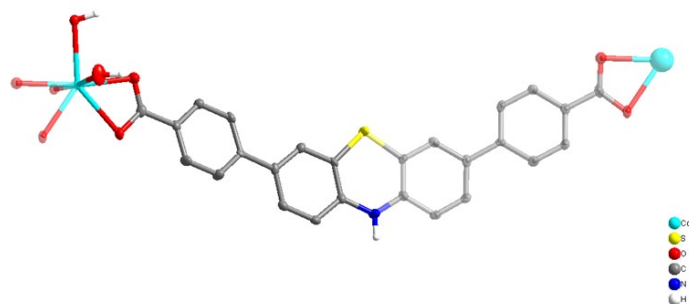
Fig. S13 The asymmetric unit of compound **Cd-PTZ-db** (The transparent atoms and fragmental bonds belong to symmetry-related part).
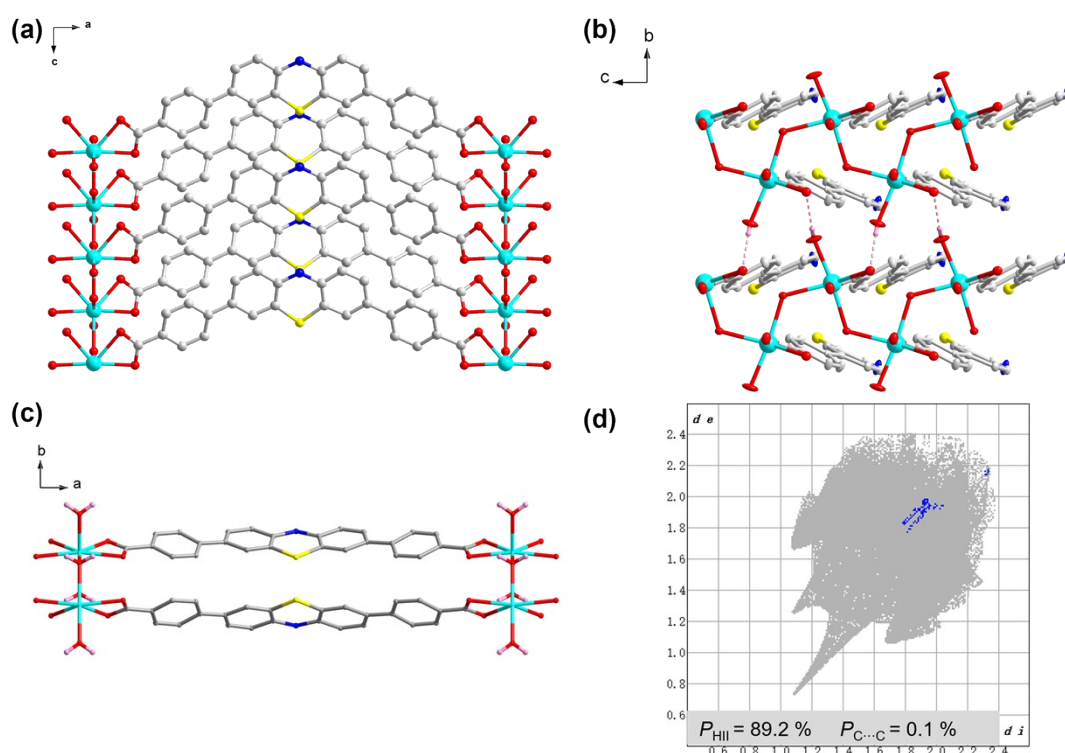

Fig. S14 The structure of **Cd-PTZ-db** seen form *b*-axis (a), *a*-axis (b) and *c*-axis (c). (Some hydrogen atoms connected to carbons and nitrogen atoms have been omitted for the sake of clarity. Color code: C, grey; O, red; N, blue; S, yellow; Cd, cyan) (d) The decomposed fingerprint plots of Hirshfeld surfaces of intermolecular C···C interaction of of **Cd-PTZ-db**. The full fingerprints appear as gray shadows underneath decomposed plots, and the intermolecular interaction is shown as a blue shadow. P_{HII} = proportion of hydrogen-involved intermolecular interaction to total intermolecular interaction; $P_{C···C}$ = proportion of intermolecular C···C interaction to total intermolecular interaction.
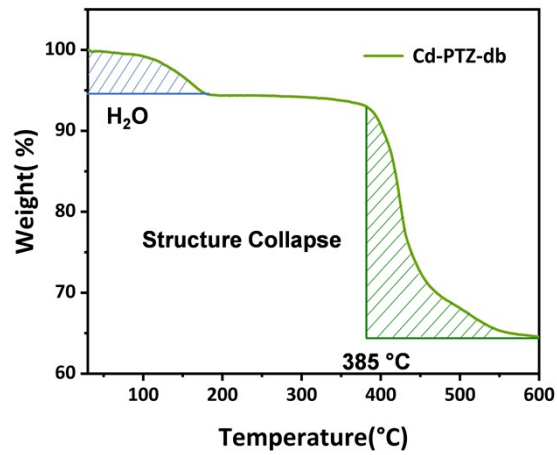
Fig. S15 The TGA curve of **Cd-PTZ-db**.
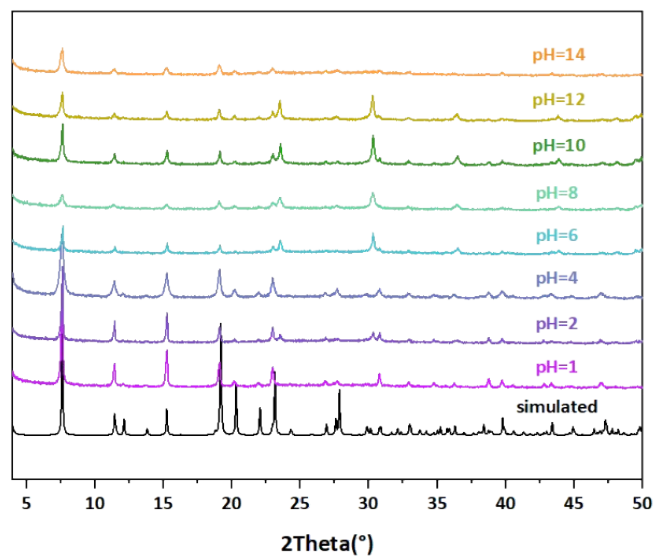
Fig. S16 PXRD patterns of **Cd-PTZ-db** after immersion in pH = 1–14 aqueous solutions.
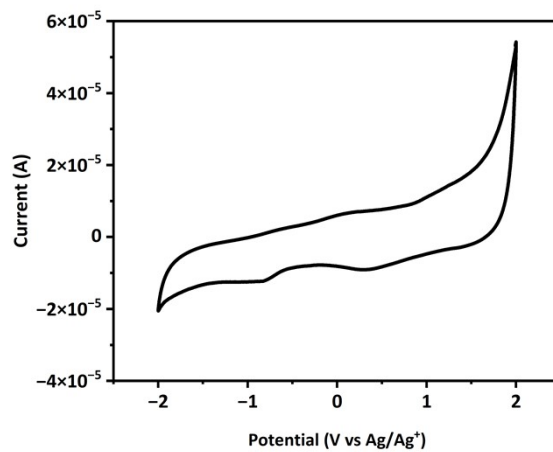
Fig. S17 Cyclic voltammograms of **Cd-PTZ-db** in the dichloromethane suspension.
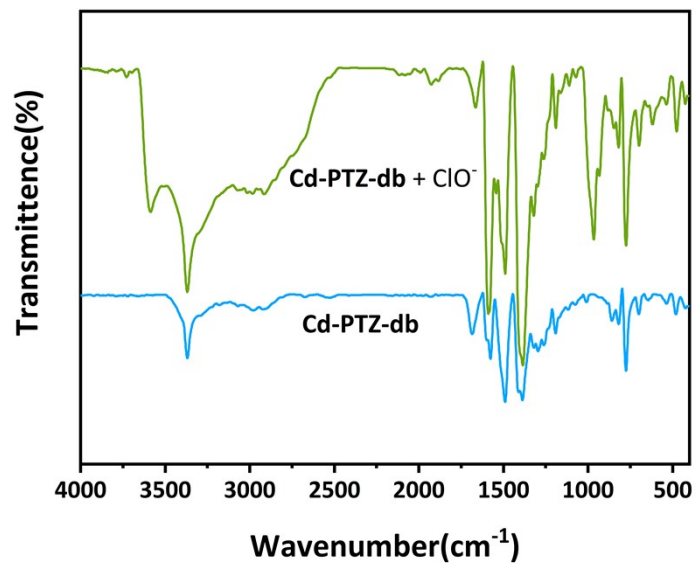
Fig. S18 FT-IR spectra of **Cd-PTZ-db** before and after adding hypochlorite.
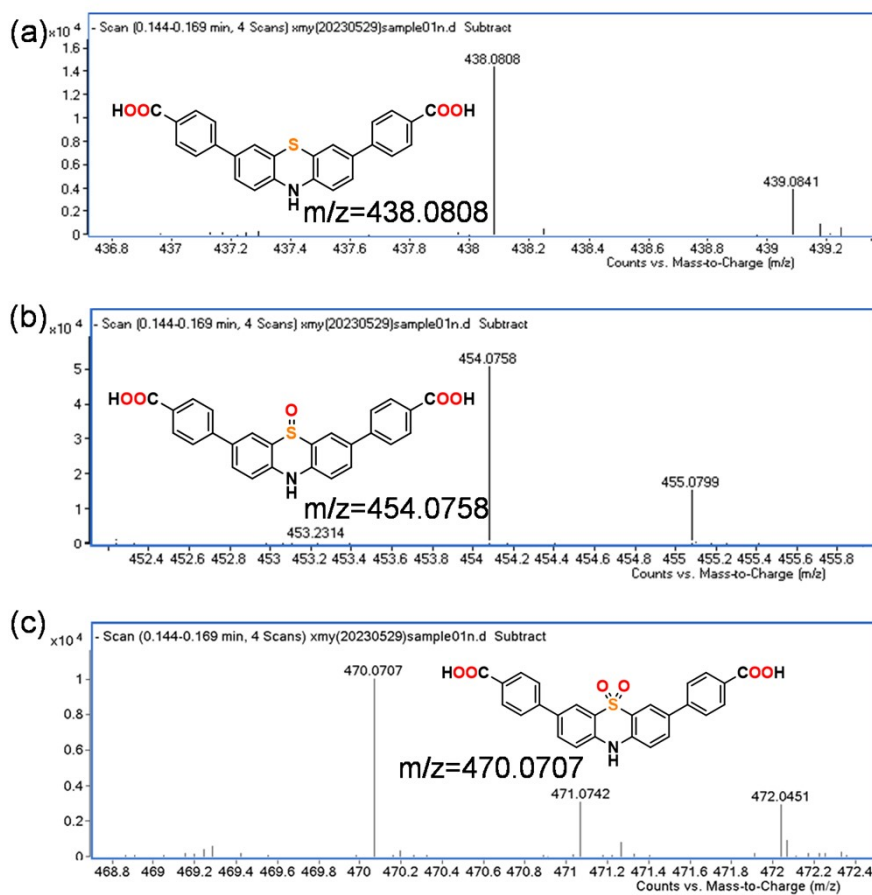
Fig. S19 HRMS spectrum of **Cd-PTZ-db**-ClO⁻.
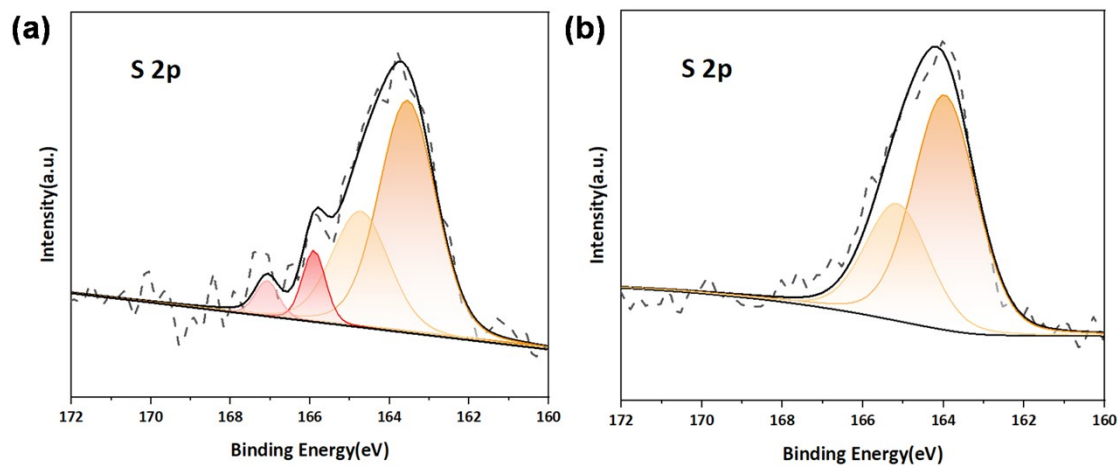
Fig. S20 S 2p XPS spectrum of **Cd-PTZ-db**-ClO⁻ (a) and **Cd-PTZ-db** (b).
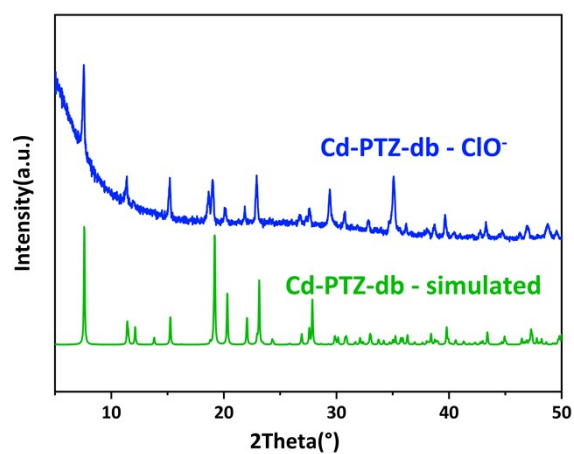
Fig. S21 PXRD patterns of compound **Cd-PTZ-db** after ClO⁻ stimulation.
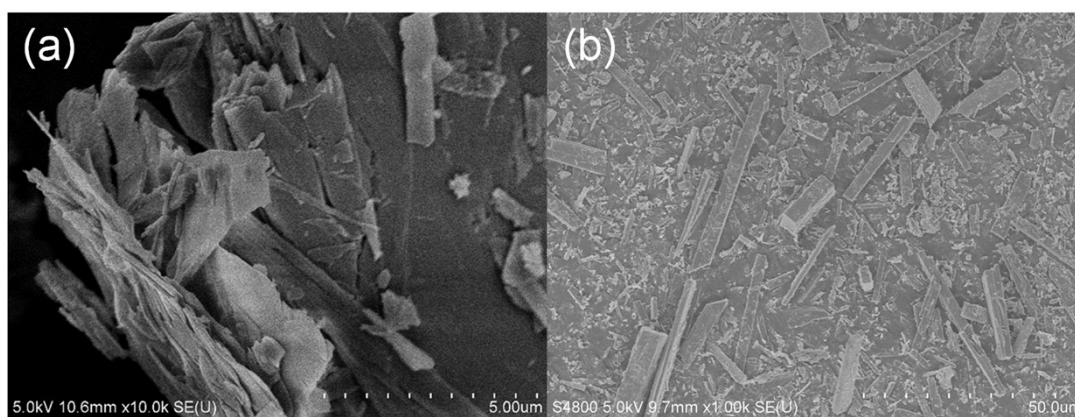
Fig. S22 SEM images of compound **Cd-PTZ-db** before (a) and after (b) the ClO⁻ stimulation
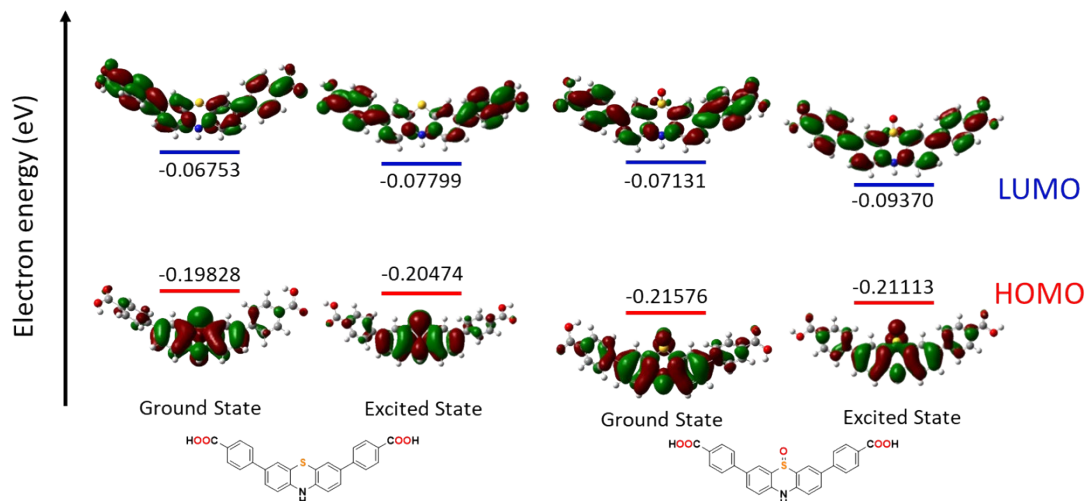
Fig. S23 Frontier molecular orbitals of H_2PTZ-dba before and after the oxidation in the ground and excited states. HOMO: highest occupied molecular orbital; LUMO: lowest unoccupied molecular orbital. Vertical excitation for the energy levels calculation was based on the optimized structures with the B3LYP method, Gaussian 09 Program.
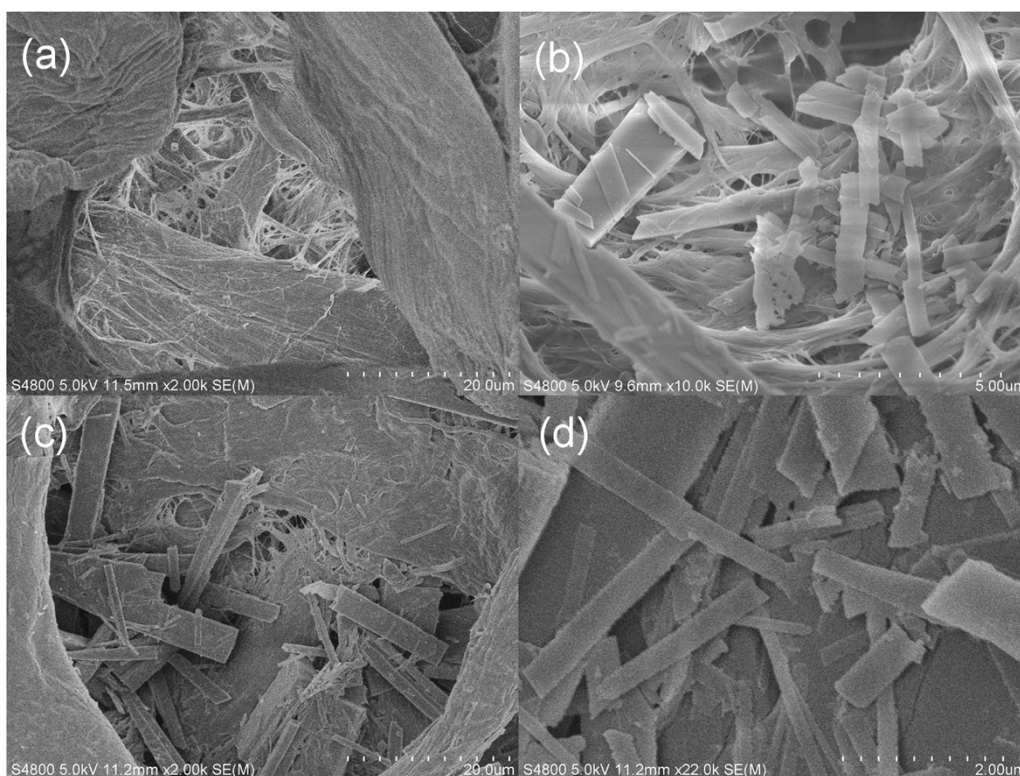
Fig. S24 SEM images of (a) blank paper strip, (b) **Cd-PTZ-db**-coated strip and (c, d) the ClO$^-$ stimulated **Cd-PTZ-db**-coated strip.

Table S1 The singlet excited state transition configurations of **PTZ-dbo** according to TD-DFT calculations. Constitution for each orbitals pair is in parentheses.

PTZ-dbo	Energy (eV)	Wavelength (nm)	Oscillator strength (f)	Transition configuration
S_1	2.4217	511.97	0.37970	H→L (81.8), H→L+2 (9.1), H→L+4 (5.6)
S_2	3.3383	371.40	0.60280	H→L+2 (73.8), H→L+6 (13.2)
S_3	3.8975	318.11	1.71880	H-1→L (62.4), H-2→L+1 (11.7), H→L+4 (8.3)

Table S2 Comparison of various ClO$^-$ probes based on MOFs.

Probe	LOD (nM)	Operation mode	Visual color change	References
Acr@Eu(BTEC)	10.75	Turn-off	Green to orange	S10
NH$_2$-Cu-MOFs	36	Turn-off	Blue	S11
AF@MOF-801	51.72	Turn-off	Green	S12
5-5-Eu/BPyDC@MOF-253-NH$_2$	94	Turn-off	Blue	S13
UiO-66-NH$_2$	63.8	Ratiometric	Blue to white	S14
ZIF-90-BA	6250	Turn-on	Green	S15
PDA/Eu/PDA-UiO-66-NH$_2$	100	Turn-on / Ratiometric	Blue-red	S16
Uio-Eu-L1	16	Turn-on	Red	S17
Cd-PTZ-db	26	Turn-on	Blue	This work

Table S3 Crystal data and refinement results for compound **PTZ-dbo** and **Cd-PTZ-db**.

	PTZ-dbo	Cd-PTZ-db
Formula	$C_{28}H_{21}NO_4S$	$C_{26}H_{19}NCdO_6S$
Formula weight	467.52	585.88
Temperature/K	193	193
Crystal system	orthorhombic	orthorhombic
Space group	$Cmc2_1$	$Pmc2_1$
a (Å)	46.915(8)	23.2254(9)
b (Å)	7.2886(11)	7.6809(3)
c (Å)	6.1504(9)	5.9740(2)
α (°)	90	90
β (°)	90	90
γ (°)	90	90
Volume (Å^3)	2103.1(6)	1065.71(7)
Z	4	2
F(000)	976	588
R1 ($I>2\sigma(I)$)	0.0815	0.0235
wR2 (reflections)	0.2103	0.0538
Goodness of fit on F^2	1.105	1.062
CCDC Number	2303468	2303469

Table S4 The selected bond lengths for compound **Cd-PTZ-db**.

Atom	Atom	Length/Å
Cd1	O3^1	2.344(3)
Cd1	O3	2.344(3)
Cd1	O4	2.402(3)
Cd1	O4^1	2.402(3)
Cd1	O1	2.390(5)
Cd1	O1^2	2.343(4)
Cd1	O2	2.225(4)

^{1}-X, +Y, +Z; ^{2}-X, 2-Y, -1/2+Z.

Table S5 The selected bond angles for compound **Cd-PTZ-db**.

Atom	Atom	Atom	Angle/°
O3[1]	Cd1	O3	167.13(18)
O3[1]	Cd1	O4[1]	55.22(18)
O3[1]	Cd1	O4	133.62(19)
O3	Cd1	O4	55.22(18)
O3	Cd1	O4[1]	133.62(19)
O3	Cd1	O1	85.91(17)
O3[1]	Cd1	O1	85.91(17)
O4	Cd1	O4[1]	78.71(16)
O1[2]	Cd1	O3[1]	85.22(10)
O1[2]	Cd1	O3	85.22(10)
O1	Cd1	O4	140.47(8)
O1	Cd1	O4[1]	140.47(8)
O1[2]	Cd1	O4	91.22(12)
O1[2]	Cd1	O4[1]	91.22(12)
O1[2]	Cd1	O1	92.43(11)
O2	Cd1	O3[1]	94.30(11)
O2	Cd1	O3	94.30(11)
O2	Cd1	O4	93.51(15)
O2	Cd1	O4[1]	93.51(15)
O2	Cd1	O1	81.46(19)
O2	Cd1	O1[2]	173.9(2)

[1]-X, +Y, +Z; [2]-X, 2-Y, -1/2+Z.

References

S1 X.-Q. Zhu, Z. Dai, A. Yu, S. Wu and J.-P. Cheng, Driving forces for the mutual conversions between phenothiazines and their various reaction intermediates in acetonitrile, *J. Phys. Chem. B,* 2008, **112**, 11694-11707.

S2 SAINT, Program for data extraction and reduction, Bruker AXS, Inc., Madison, WI, 2001.

S3 G. M. Sheldrick, SADABS, University of Göttingen, Göttingen, Germany, 2003.

S4 G. M. Sheldrick, *SHELXT* – Integrated space-group and crystal-structure determination, *Acta Cryst. A*, 2015, **71**, 3-8.

S5 G. M. Sheldrick, Crystal structure refinement with *SHELXL*, *Acta Cryst. C*, 2015 ,**71**, 3-8.

S6 M. J. Frisch, G. W. Trucks, H. B. Schlegel, G. E. Scuseria, M. A. Robb, J. R. Cheeseman, G. Scalmani, V. Barone, G. A. Petersson, H. Nakatsuji, X. Li, M. Caricato, A. V. Marenich, J. Bloino, B. G. Janesko, R. Gomperts, B. Mennucci, H. P. Hratchian, J. V. Ortiz, A. F. Izmaylov, J. L. Sonnenberg, D. Williams-Young,

F. Ding, F. Lipparini, F. Egidi, J. Goings, B. Peng, A. Petrone, T. Henderson, D. Ranasinghe, V. G. Zakrzewski, J. Gao, N. Rega, G. Zheng, W. Liang, M. Hada, M. Ehara, K. Toyota, R. Fukuda, J. Hasegawa, M. Ishida, T. Nakajima, Y. Honda, O. Kitao, H. Nakai, T. Vreven, K. Throssell, J. A. Montgomery, Jr., J. E. Peralta, F. Ogliaro, M. J. Bearpark, J. J. Heyd, E. N. Brothers, K. N. Kudin, V. N. Staroverov, T. A. Keith, R. Kobayashi, J. Normand, K. Raghavachari, A. P. Rendell, J. C. Burant, S. S. Iyengar, J. Tomasi, M. Cossi, J. M. Millam, M. Klene, C. Adamo, R. Cammi, J. W. Ochterski, R. L. Martin, K. Morokuma, O. Farkas, J. B. Foresman, and D. J. Fox, Gaussian, Inc., Wallingford CT, 2016.

S7 H. T. Sun, Z. B. Hu, C. Zhong, X. K. Chen, Z. R. Sun and J.-L. Brédas, Impact of dielectric constant on the singlet–triplet gap in thermally activated delayed fluorescence materials, *J. Phys. Chem. Lett.,* 2017, **8**, 2393–2398.

S8 M. J. Abraham, T. Murtola, R. Schulz, S. Páll, J. C. Smith, B. Hess and E. Lindahl, GROMACS: High performance molecular simulations through multi-level parallelism from laptops to supercomputers, *SoftwareX*, 2015, **1-2**, 19-25.

S9 N. Schmid, A. P. Eichenberger, A. Choutko, S. Riniker, M. Winger, A. E. Mark and W. F. van Gunsteren, Definition and testing of the GROMOS force-field versions 54A7 and 54B7, *Eur. Biophys. J.*, 2011, **40**, 843-856.

S10 J. Xiong, Y. F. Xiao, J. M. Liang, J. Sun, L. X. Gao, Q. J. Zhou, D. Hong and K. J. Tan, Dye-based dual-emission Eu-MOF synthesized by post-modification for the sensitive ratio fluorescence visualization sensing of ClO⁻, *Spectrochim. Acta A,* 2023, **285**, 121863.

S11 P. P. Huo, Z. J. Li, C. B. Fan and S. Z. Pu, Amino-functionalized copper-based metal–organic frameworks for highly selective and sensitive detection of hypochlorite, *New J. Chem.,* 2020, **44**, 19753-19758.

S12 Y. X. Ye, L. W. Zhao, S. G Hu, A. J. Liang, Y. S. Li, Q. X. Zhuang, G. R Tao and J. L. Gu, Specific detection of hypochlorite based on the size-selective effect of luminophore integrated MOF-801 synthesized by a one-pot strategy, *Dalton Trans.,* 2019, **48**, 2617-2625.

S13 Y. N. Zeng, H. Q. Zheng, J. F. Gu, G. J. Cao, W. E. Zhuang, J. D. Lin, R. Cao, and Z. J. Lin, Dual-emissive metal–organic framework as a fluorescent "switch" for ratiometric sensing of hypochlorite and ascorbic acid, *Inorg. Chem.,* 2019, **58**, 13360-13369.

S14 F. F. Yu, T. Y. Du, Y. H. Wang, C. M. Li, Z. J. Qin, H. Jiang and X. M. Wang, Ratiometric fluorescence sensing of UiO-66-NH₂ toward hypochlorite with novel dual emission in vitro and in vivo, *Sensors. Actuat. B-chem.,* 2022, **353**, 131032.

S15 Y. P. Li, K. Jiang, J. Zhang, T. F Xia, Y. J. Cui, Y. Yang and G. D. Qian, A turn-on fluorescence probe based on post-modified metal–organic frameworks for highly selective and fast-response hypochlorite detection, *Polyhedron,* 2018, **148**, 76-80.

S16 Y. N. Zeng, H. Q. Zheng, X. H. He, G. J. Cao, B. Wang, K. C. Wu and Z. J. Lin, Dual-emissive metal–organic framework: a novel turn-on and ratiometric fluorescent sensor for highly efficient and specific detection of hypochlorite, *Dalton Trans.,* 2020, **49**, 9680-9687.

S17 Z. Zhou, X. Q. Li, Y. P. Tang, C. C. Zhang, H. R. Fu, N. T. Wu, L. F. Ma, J. W. Gao and Q. M. Wang, Oxidative deoximation reaction induced recognition of hypochlorite based on a new fluorescent lanthanide-organic framework, *Chem. Eng. J.,* 2018, **351**, 364-370.